NeuroImage 49 (2010) 2494–2502

Contents lists available at ScienceDirect

NeuroImage

journal homepage: www.elsevier.com/locate/ynimg

The folding fingerprint of visual cortex reveals the timing of human V1 and V2

Justin Ales *, Thom Carney, Stanley A. Klein

UC Berkeley, Optometry, 360 Minor Hall, Berkeley, CA 94720, USA

ARTICLE INFO

Article history:
Received 6 July 2009
Revised 11 September 2009
Accepted 15 September 2009
Available online 22 September 2009

ABSTRACT

Primate neocortex contains over 30 visual areas. Recent techniques such as functional magnetic resonance imaging (fMRI) have successfully identified many of these areas in the human brain, but have been of limited value for revealing the temporal dynamics between visual areas. The electroencephalogram (EEG) provides information with high temporal precision, but has had limited success separating out the signals from individual neighboring cortical areas. Consequently, controversies exist over the temporal dynamics across cortical areas. In order to address this problem we developed a new method to identify the sources of the EEG. An individual's unique cortical pattern of sulci and gyri along with a visual area's functional retinotopic layout provides a folding fingerprint that predicts specific scalp topographies for stimuli presented in different parts of the visual field. Using this folding fingerprint with a 96 or 192 location stimulus severely constrains the solution space making it relatively easy to extract the temporal response of multiple visual areas to multiple stimulus locations. The large number of stimuli also provides a means to validate the waveforms by comparing across stimulus sets, an important feature not present in most EEG source identification procedures. Using this method our data reveal that both V1 and V2 waveforms have similar onset latencies, and their temporal dynamics provide new information regarding the response latencies of these areas in humans. Our method enables the previously unattainable separation of EEG responses from neighboring brain areas. While we applied the method to the first two cortical visual areas, V1 and V2, this method is also applicable to somatosensory areas that have defined mappings. This method provides a means to study the rapid information flow in the human brain to reveal top-down and bottom-up cognitive processes.

Introduction

fMRI has provided exquisite spatial maps of visual cortex (Baseler et al., 1999; DeYoe et al., 1994; Engel et al., 1997). Early visual areas V1 and V2 follow a retinotopic layout such that adjacent positions in the observer's visual field activate adjacent regions of cortex. The fMRI signal has a time course on the order of seconds, hence the method's poor temporal resolution. Electroencephalography (EEG), on the other hand, measures the electrical activity generated by the brain with a temporal resolution on the order of 10^{-3} s. This is three orders of magnitude faster than fMRI and is a direct measure of neural activity. The problem has been to identify the individual responses of the multiple sources that account for the summed activity recorded from the scalp.

The two most widely used classes of methods are multiple dipole modeling and distributed source imaging. Unfortunately, for both methods, closely spaced sources, such as between cortical areas V1 and V2, are impossible to differentiate. Multiple dipole modeling involves a nonlinear search on the parameters of a few point sources (Scherg, 1992). The process runs into problems when sources are close because a single rotating source can do an adequate job of fitting the data generated by multiple closely spaced sources (Zhang et al., 1994). The source imaging method (often called minimum norm methods) on the other hand, fixes many sources onto the cortical surface given by an MRI and estimates the activation of those sources (Dale et al., 2000; Hämäläinen and Ilmoniemi, 1994; Phillips et al., 2002). Source imaging has the drawback of producing sources that are excessively spread out. While methods have been proposed to focus the source solutions by applying further constraints from, for example, fMRI data these methods still have problems with source crosstalk (Dale et al., 1999).

Relatively few studies have used fMRI to quantify localization error of EEG/MEG. A pair of studies compared fMRI localization to dipole source localization using EEG (Baker et al., 2006; Sharon et al., 2007) using both MEG and EEG. In both cases the focus was on the dominant dipole, assumed to be localized in V1. Both studies came to a very similar conclusion that the deviation of the best fitting EEG dipole source locations from the expected fMRI locations had a mean error ranging from 13–16 mm for four hemispheres (Baker et al) to 12–15 mm for 3 hemispheres with a fourth hemisphere having an error of 53 mm (Sharon et al., 2007). When Sharon et al. supplemented the EEG signal with MEG localization the range reduced to a 5- to 8 -mm error compared to fMRI for a single V1 source.

* Corresponding author.
E-mail addresses: ales@berkeley.edu, justin.ales@gmail.com (J. Ales).

1053-8119/$ – see front matter © 2009 Elsevier Inc. All rights reserved.
doi:10.1016/j.neuroimage.2009.09.022

Several studies have shown that adequate source separation depends on several factors such as: signal to noise ratio, proper forward model, and source orientation (Baillet et al., 2001; Ferree et al., 2001; Lütkenhöner, 1998). Under typical conditions a minimum separation of 4 cm is needed to resolve sources. When sources are not resolvable they can mix together, a phenomena called the cross-talk (Dale et al., 1999), or the rotation problem (Dandekar et al., 2007; Klein and Carney, 1995). This problem refers to the fact that when sources are not sufficiently separated it is impossible to determine if the reconstructed source time functions are pure or mixtures of the true time functions.

To resolve close sources additional information needs to be incorporated into the method (Hagler et al, 2008). The solution described in this paper uses an individual's unique cortical shape within visual areas V1 and V2, the folding fingerprint, to solve the problem of identifying the source time functions. Moreover, the method provides a means of validating the identified temporal responses by comparing results across stimulus locations. The method utilizes the subjects' known retinotopy, given by fMRI, to help constrain the sources' spatial location and orientation. The crucial aspect of this method for obtaining separation between visual areas is the assumption that the temporal response within a visual area is the same across multiple stimulus locations. The method can be extended to additional retinotopic visual areas with suitable elaboration of the MRI and fMRI topographies. The use of the folding fingerprint of cortical areas disambiguates the activity of nearby sources and enables the accurate characterization of the where and when of visual cortex activation in the human brain.

Methods

Data were collected from two healthy volunteer, male subjects. Subjects gave written informed consent, and safety guidelines were followed as approved by the Committee for the Protection of Human Subjects at the University of California, Berkeley.

fMRI

Magnetic resonance images were acquired at Stanford University using a 3-T GE Signa scanner. A special-purpose semicylindrical surface coil around the back of the head was used. Functional magnetic resonance images were oriented parallel to the calcarine sulcus. Eight functional images were acquired every 3 s using a two-shot, two-dimensional spiral gradient-recalled echo sequence; voxel size was $2\times2\times3$ mm. Structural (T1-weighted) images were acquired in the same planes and with the same resolution as the functional images to coregister the functional and anatomical data.

fMRI stimulus

The stimulus for the fMRI experiments consisted of clockwise rotating wedges and expanding annuli with a cycle of 72 s, resulting in five complete cycles during the 6-min stimulus presentation. The wedge and ring were comprised of a flickering (reversal rate of 8 Hz) checkerboard (Engel et al., 1997). The stimulus presentation was repeated 4 times for each. Analysis tools standard to many vision fMRI groups were used for mapping the visual cortex. The three-dimensional cortex was unfolded onto a two-dimensional flat map to better view the retinotopic data. White matter segmentation was performed to ensure a continuous gray matter surface for unfolding. The white matter segmentation and unfolding were done using the FreeSurfer software package (Dale et al., 1999; Fischl et al., 1999). The Stanford mrVISTA tools were used to analyze and project the fMRI data onto the flat maps (Teo et al., 1997). The results of this data analysis are shown in Fig. 1a for the left hemisphere of subject 1, and in Fig. 2a for subject 2. The colormap is the phase plot of the rotating wedge stimulus. To define initial locations for the EEG sources, described below, mrVISTA was used to define polygonal ROI's with linearly interpolated wedge and ring retinotopic maps. Using these polygonal ROI's we defined the fMRI response phase at the foveal confluence to the fovea. These atlas maps provided the location for the EEG sources.

EEG data

Subjects were comfortably seated in a dark sound-attenuating chamber. Electroencephalograms were continuously recorded with the Biosemi EEG ActiveTwo system (www.biosemi.com) while wearing a cap with 96 active electrodes. The 96-channel cap layout was custom designed to achieve a high density of electrodes around the occipital bone. EEG data were collected at a sampling rate of 512 Hz, and later digitally filtered with a pass band of 2–100 Hz. Along with the EEG, stimulus synchronization pulses generated by the WinVis neurophysiological testing platform (www.neurometrics.com/winvis) were recorded for offline data analysis. Each run was divided into 1 min recording periods, each separated by a subject-defined rest interval. The time required to acquire the EEG data required collecting data across multiple days. In order to reduce the variability of electrode positioning the cap was carefully applied. On each application the inion, nasion, and periauricular points were found, and electrodes were placed known distances from these fiducial reference points. Midline electrodes were placed along the inion-nasion axis, and measured to ensure the line was halfway between the periauricular points. After the final recording session the electrode locations were digitized using a Polhemus FASTRAK system. In addition, in order to help the registration, about a hundred points randomly distributed around the head were digitized. These points were then aligned to the MRI coordinates by using the surface of the scalp. The forward modeling was calculated using a 3-shell spherical model. The error introduced by using a spherical shell model instead of a boundary element model is likely minimal. Since all dipole locations are within a few centimeters of each other the differential effect of location is smaller than that of orientation. The outer radius of the sphere was chosen to best fit the electrode locations and the thicknesses for the 3 shells were chosen to fit those observed from the MRI. Scalp, skull, brain conductivity values used were 0.33 S/m, 0.01 S/m, 0.33 S/m, respectively (Goncalves et al., 2003). Forward model calculations were done using the Brainstorm Matlab toolbox (Mosher et al., 1993; Mosher et al., 1999; Zhang, 1995). The surface EEG reflects the current flow along pyramidal cell dendrites that are oriented perpendicular to the cortical surface (Nunez and Srinivasan, 2006). Therefore, the orientation of the dipole current sources is assumed to be normal to the reconstructed white to gray matter boundary so we constrained our source dipoles to be on the gray/white boundary with a fixed orientation normal to the surface.

Multifocal EEG stimuli

The stimuli were presented on a CRT monitor with 1024×768 pixel resolution at a viewing distance of 110 cm. The background luminance was 2.9 candelas/m^2 and patch contrast was 99%. Mean patch luminance was 16 candelas/m^2. The stimulus dartboard pattern defined an annulus with an inner radius of 1 degree and an outer radius of 8.5 degrees. The pattern within this annulus for one observer was a dartboard divided into 8 rings of 24 patches (192 patches see Fig. 3 left side) these rings had borders at a radius of 1.5, 2.2, 2.9, 3.5, 4.5, 5.5, and 7.2 degrees of visual angle. The second observer's stimulus had 4 rings of 24 patches (Fig. 3 right side) these rings had borders at a radius of 2.2, 3.5, and 5.5 degrees of visual angle. Each patch was a 2×2 or 2×4 checkerboard for the 192 and 96 patch stimuli. Based on estimates of human cortical magnification the width of each ring was adjusted so that each ring activated approximately equal areas of primary cortex (Carney et al., 2006; Horton and Hoyt, 1991).

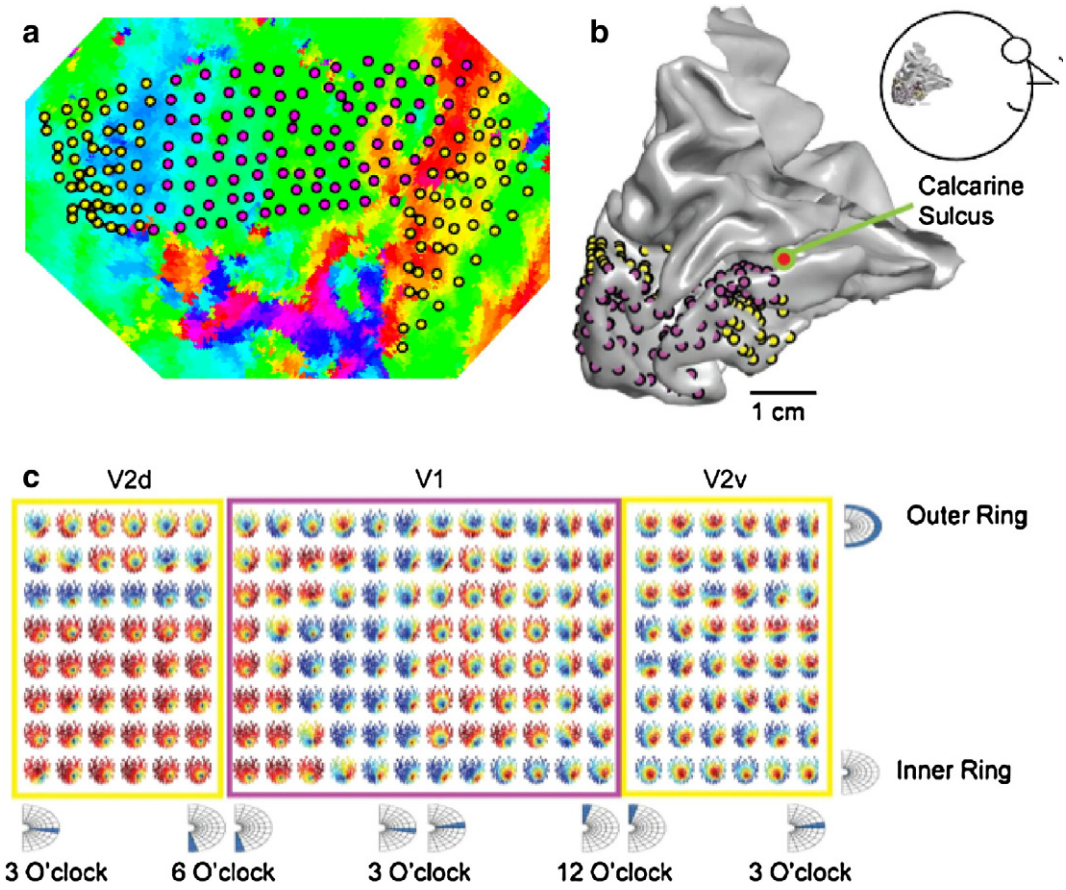

Fig. 1. Illustration of combining fMRI and EEG retinotopic maps. This figure illustrates a complete left hemisphere mapping for subject 1. Panel a shows the fMRI data overlaid with the initial V1 (in magenta) and V2 (in yellow) source locations for the 96 stimulus patches in this hemisphere. Panel b shows how this mapping gets translated onto the folded cortical surface. Adjacent tangent V1 sources are separated by about 3.5 mm which is consistent with prior estimates(Carney et al., 2006; Dougherty et al., 2003; Schira et al., 2007). Panel c contains scalp topographies for V1/V2 sources for all 96 stimulus patches. Each one of the topographies is a flattened representation of the 96 electrodes, with the subject's nose toward the top. The scalp topographies are laid out retinotopically, in the same manner as the fMRI data of panel a. The topographies are the final V1/V2 topographies after the constrained search as described in the text.

The 192 (or 96) patches were simultaneously and independently pattern reversed according to an m-sequence using a standard multifocal paradigm (Sutter, 2001). The WinVis stimulus delivery software ensures presentations with perfect synchronization, free of frame drops and with flexible stimulus design (Carney et al., 2006). The multifocal stimulus allowed us to separate out the responses for each individual stimulus patch location. A 16-bit m-sequence was used, corresponding to 65535 video frames. The stimulus was presented at 60 Hz for a run time of 18.2 min per sequence. In order to get a sufficient signal to noise ratio from all the extremely small 196 patch stimuli the run had to be repeated 25 times. The 25 replications took required approximately 500 min of recording that was spread over 5 days. The 96-patch stimulus required a single recording session of 120 min consisting of 6 repeats (since patches with twice the area require 1/4 the number of trials to get the same signal to noise ratio). We calculated signal to noise ratio as the ratio of root-mean-square (RMS) amplitude in the time window 90 to 180 ms post-stimulus, with a prestimulus time window of the same length. 21–23. Across all stimulus locations the mean SNR for subject 1 was 2.1. The best stimulus location had a high of 4.2 with the worst having an SNR of 1.1. Subject 2 had a mean SNR 3.2, with a high of 5.3 and a low of 1.4. We resampled the data to have an integer number of 9 samples per video frame, which results in a sampling rate of 540 Hz. We then extracted the responses corresponding to the pattern reversal of the checkerboard patch using the fast Walsh transform; in the multifocal literature it is referred to as the first cut of the second order kernel (Sutter, 1991).

New source identification methods

This subsection presents a new method that is critical for our goal of disambiguating temporal responses from V1 and V2. Because these areas are adjacent, standard localization methods have failed to adequately differentiate them. However, much is known anatomically and physiologically about these areas. One good source of information is the retinotopic mapping of each of the areas. The source identification method presented in this paper rests on two assumptions about the multifocal EEG data. One, EEG sources from V1 and V2 are retinotopically organized and consistent with an individual subject's fMRI map. Two, at a fixed eccentricity, sources within a visual area have the same response. We have previously made this assumption in fitting single dipoles (Slotnick et al., 1999). The second assumption is partially supported both by the results in Baseler and Sutter (1997) and also by our results (see Fig. 7) that show very similar estimates of the V1 and V2 time functions which were extracted separately from each hemisphere for the same stimulus eccentricity. The common time function assumption is crucial for obtaining separation of closely spaced sources. However, if the response varies as a function of stimulus location at the same eccentricity the algorithm will fit the underlying mixture of responses with only a single time course.

The multifocal data are able to exploit these *a priori* assumptions because it contains separate responses from multiple stimulus locations. However, this multiplicity of responses brings

with it data analysis challenges. The basic equation that we use is:

$$V_{pred}\left(\mathbf{d}_{e,p},t\right)=\sum_s A\left(\mathbf{d}_{e,p},s\right)T(s,t) \quad (1)$$

The matrix A is the forward model matrix that specifies the voltages at the scalp. A is indexed by $\mathbf{d}_{e,p}$ which combines into a single index the electrodes (e) and stimulus locations, or patches (p). The electrodes (e) range from 1 to 96, and the patches (p) range from 1 to 192 for subject 1 and 1 to 96 for subject 2. In the actual fitting we do 12 patches in a hemi-ring at a time to enable validation. We are especially concerned with comparing hemi-rings of the right and left visual field at a given eccentricity where the temporal responses are expected to be the same. The second dimension of A is (s), the source visual area (V1 or V2). Finally, (t) specifies the time samples (1 to 161 corresponding to 296 ms). The goal of our algorithm is to determine $A(\mathbf{d}_{e,\ p},s)$ and $T(s,\ t)$ that will minimize the sum of square error cost function with dipole location constrained by fMRI and dipole orientation constrained by MRI:

$$SSE=\sum_{de,p,t}\left(V_{pred}\left(\mathbf{d}_{e,p,}t\right)-V_{EEG}\left(\mathbf{d}_{e,p},t\right)\right)^2 \quad (2)$$

where V_{pred} is from Eq. (1) and V_{EEG} is our multifocal evoked potential data. Note that for any given time point there are 16 and 8 hemi-rings for subjects 1 and 2 with each hemi-ring having N_e $N_p=\ 96\times12$ data.

The fMRI predicted topographies are a source of noise. Small errors in identifying a patch location near a cortical fold can result in a poor estimate of the scalp topographies for that patch. To reduce this type of error the linear regression was iterated with the individual source locations constrained to a 5×5 mm box centered on the fMRI defined initial location, in order to find the match that minimized the residual error with respect to the recorded VEPs. The topographies, shown in Figs. 1c and 2c, are the ones that are predicted by the MRI after optimization of source locations on the fMRI map. The signal strength at the scalp for a dipole with an orientation pointed away from the white matter is color coded from blue (for positive voltage) to red (for negative voltage).

The following is a more detailed stepwise overview of the source identification procedure.

Step 1. Get initial mapping of V1 and V2 from fMRI data corresponding to the patches used in the EEG stimulus (Figs. 1a and 2a for subjects 1 and 2). The locations on the flat map are used for matching source location with the fMRI, and the 3d MRI based reconstruction is used to extract source orientations (Figs. 1b and 2b). Given these locations and orientation the forward model solutions for the voltages on the scalp can be predicted (Figs. 1c and 2c). This fMRI predicted topography forms the matrix $A(\mathbf{d}_{e,p},s)$. For ease of visual inspection the matrix is represented in the following form. The index over electrodes (e) is grouped into a flattened representation of the electrode positions on the scalp. The indices over patch locations (p) and visual area (s) are ordered consistent with the retinotopic layout of the stimulus. These topographies are normalized to unity to avoid biasing the matrix inversion solution procedure by relatively large, or small, predicted topographies. Note the signal distribution for a particular visual area typically changes slowly from patch to patch, even though no smoothing has been done in data acquisition or data processing. In areas where the source moves around a sulcus the predicted surface topography for corresponding stimulus patches changes rapidly.

Step 2. Given the present guess for dipole locations do a linear regression to find the two source time functions: $T(s,t)$)

$$T(s,t)=PA\left(s,\mathbf{d}_{e,p}\right)V_{EEG}\left(\mathbf{d}_{e,p}t\right) \quad (3)$$

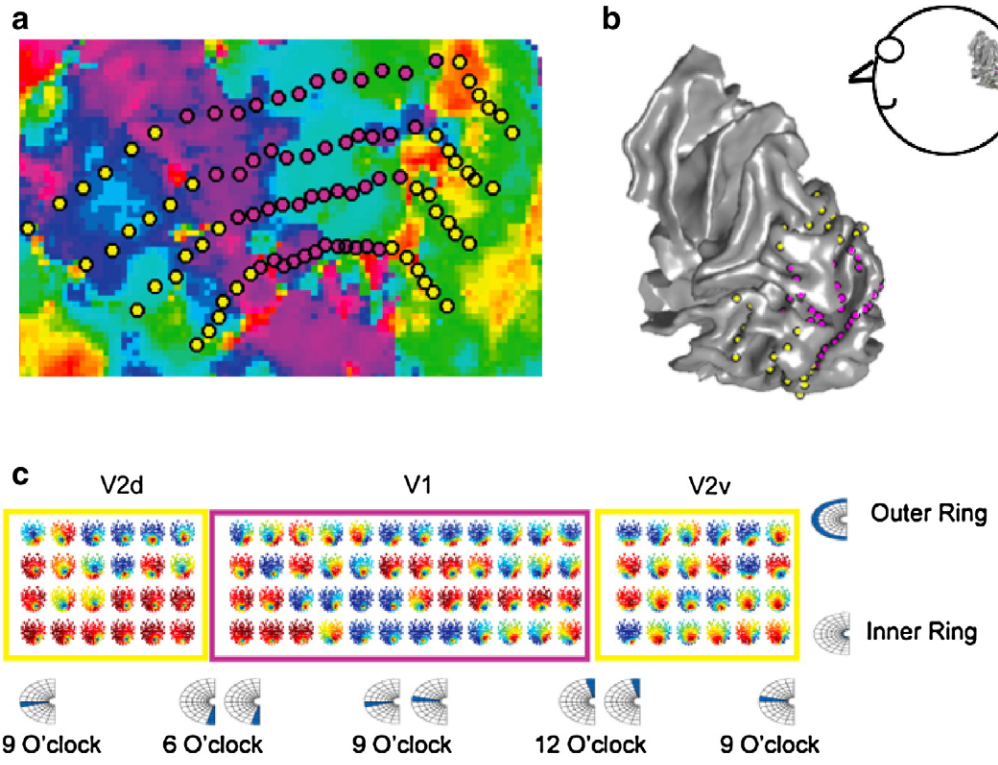

Fig. 2. Illustration of combining fMRI and EEG retinotopic maps. This figure illustrates a complete left hemisphere mapping for subject 2. Panel a shows the fMRI data overlaid with the initial V1 (in magenta) and V2 (in yellow) source locations for the 48 stimulus patches in this hemisphere. Panel b shows how this mapping gets translated onto the folded cortical surface. Panel c contains scalp topographies for V1/V2 sources for all 48 stimulus patches. Each one of the topographies is a flattened representation of the 48 electrodes, with the subject's nose toward the top. The scalp topographies are laid out retinotopically, in the same manner as the fMRI data of panel a. The topographies are the final V1/V2 topographies after the constrained search as described in the text.

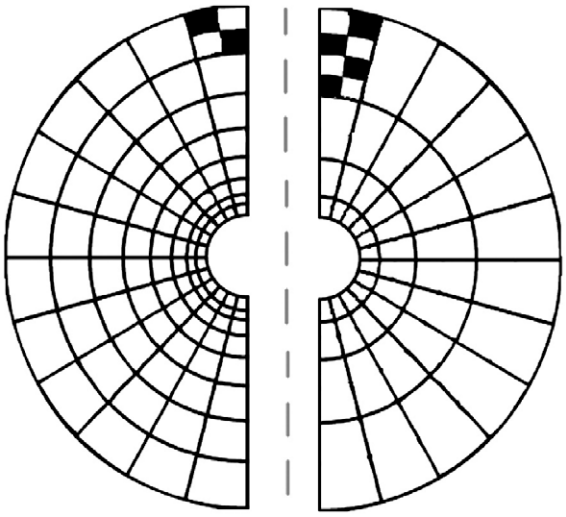

Fig. 3. Stimulus layout. This shows a schematic layout of the stimulus. The outline on the left shows the 192 patch/8 ring stimulus, while the outline on the right shows the 96 patch/4 ring stimulus. Each of the outlined areas above contained a black and white checkerboard pattern (see example in the top patch) that was pattern reversed as a unit according to the multifocal stimulus.

PA is the pseudo-inverse of A, given by:

$$\mathrm{PA} = \left(\mathrm{A}^{\mathrm{T}}\mathrm{A}\right)^{-1}\mathrm{A}^{\mathrm{T}}. \tag{4}$$

The pseudo-inverse is the matrix method for doing linear regression for minimizing SSE of Eq. (2) for the case of independent, equally weighted data. PA is simply a 2×2 matrix times the forward model, A. This step gives the best time function fit to the full dataset based on the dipole orientations specified by the MRI topography. This is the step where having multiple patches is important for having sufficient orthogonality between the multiple sources.

Step 3. For each stimulus patch, p, do an exhaustive grid search of the dipole location over the tessellated cortical surface mesh points of Figs. 1a and 2a, that are within a box 5 mm on a side centered on the original fMRI placement. This constraint limits the dipole location to be within one fMRI voxel length of the initial estimate. Using the time function from Step 2 and the electrode potential for each grid search dipole location, calculate the predicted data, $V_{\mathrm{pred}}(\mathbf{d}_{\mathrm{e,p}}, t)$ using Eq. (1). Pick the location for each patch that minimizes the sum of square error between the raw data and the predicted data as specified by Eq. (5).

$$\mathrm{SSE(p)} = \sum_{\mathrm{d,t}}\left(\mathrm{V_{pred}}\left(\mathbf{d}_{\mathrm{e,p}},\mathrm{t}\right) - \mathrm{V_{EEG}}\left(\mathbf{d}_{\mathrm{e,p}},\mathrm{t}\right)\right)^2 \tag{5}$$

It is important to realize that Eq. (5) differs from Eq. (2) in that p is not summed over. By doing the grid search patch by patch the dipole location search becomes computationally feasible. Each iteration can give a slightly different optimal value of flat map locations because the time functions are shifting across iterations (Eq. 3).

Step 4. Go to step 2 using the new optimal dipole locations from Step 3. Keep iterating until the SSE converges to a minimum. It should be noted that the source locations are never allowed to move more than 3.5 mm from the initial locations found in Step 1. At most 10 iterations were needed for convergence.

Fig. 4 shows the flattened fMRI map colored according to surface curvature, negative is light colored and positive curvature is dark. On top of the curvature map are both the pre-search (V1 in yellow, and V2 in red) and post-search (V1 in black and V2 in blue) dipole locations. The pre and post locations are connected with a line. One of the main points of this figure is that the magnitudes of the dipole shifts are visible. The amount of shifting is shown in the histogram plotted separately in Fig. 5 for each subject. The average shift on the flat-map is 2.47 ± 0.4 mm, with the minimum possible shift being 0 and maximum being about 3.5 mm. We also tried various other similar values for the constraint and obtained similar results. However, large search areas, greater then 10 mm, resulted in significantly worse cross hemisphere validation results. We might expect that on flat regions of cortex the dipole location is highly uncertain so the dipole would wander to a relatively random location within the constrained square. However, if the forward model were misspecified (as is surely the case since skull/scalp conductivity is not certain) the dipole would seek out a region with the appropriate orientation. This could produce bunching of dipoles from neighboring patches that are seeking the same orientation. One can think of our cortically constrained search as a method for limiting the dipole orientation to values that are consistent with the MRI surface normal in the region of one or two fMRI voxels. Sharon et al. (2007) compared dipole source locations to fMRI locations, very similar to the approach of Baker et al. (2006). Sharon et al. (2007) allowed the dipole orientation to be constrained within a factor 0.6 of the MRI cortical normal. Our constraint is more restrictive then Sharon et al. because it only allows orientations that are within the local region.

Results

Fig. 6 shows the V1 and V2 time functions for each hemi-ring of stimulus patches for two subjects before the cortically constrained search. The left and right hemisphere temporal functions are plotted in blue and red, respectively. As described in the methods, our forward model is unit normalized, therefore our time functions become unitless. The plots in Fig. 6 are normalized to be on

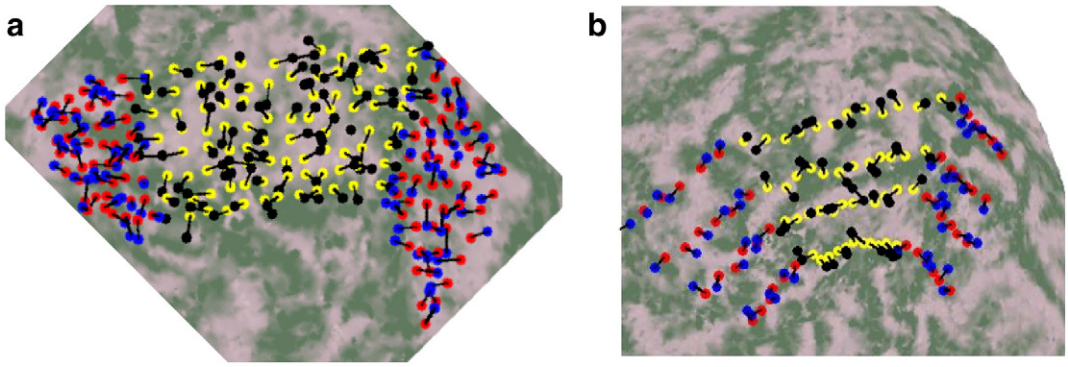

Fig. 4. Movement of dipoles on cortex after search. This figure shows the initial locations for V1 sources in yellow, along with their final positions in black. The initial V2 locations are in red, and the final locations after the search are in blue. Subject 1 is in panel a, and subject 2 is in panel b.

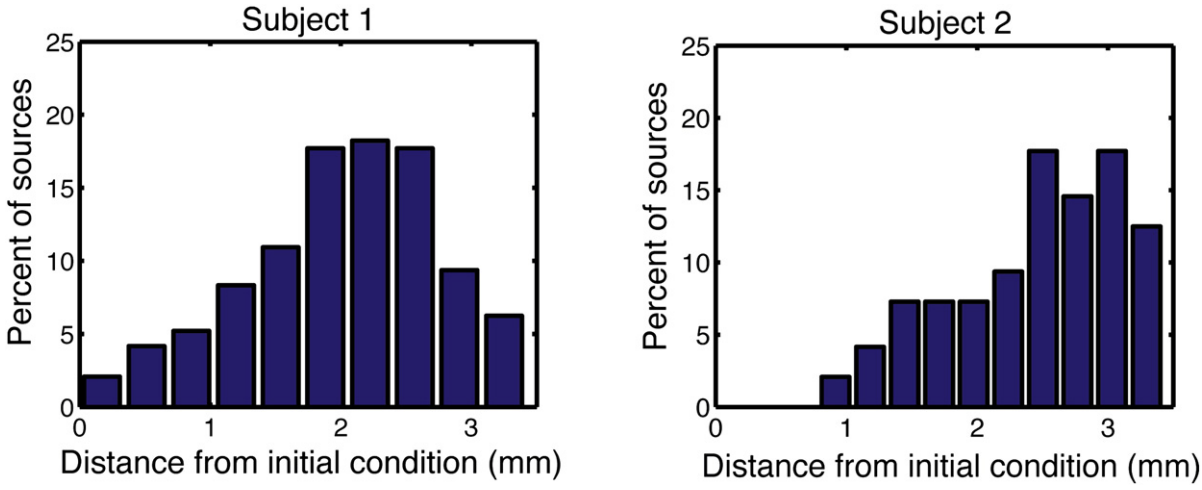

Fig. 5. Histogram of the distance dipoles moved during search. This figure shows the distribution of movements from the initial fMRI conditions.

the same scale as those in Fig. 7. The waveforms are plotted with positive representing a dipole pointing out, away from the cortex, and negative representing a source pointing in. The results shown are for the 8 stimulus rings viewed by subject 1 and for the 4 rings viewed by subject 2. The left and right hemisphere responses for areas V1 and V2 are expected to be the same within a subject (Dandekar et al., 2007). This provides an internal validation of the solution set since the hemi-ring data from each hemisphere, with their unique cortical folding patterns, are independently processed. To quantify the cross hemisphere similarity we calculated the percent RMS error between the two waveforms. This number is plotted in front of each waveform. The lack of agreement between the left and right hemisphere responses was the motivating factors to develop the iterative search algorithm described in the methods. The search was used because the large number of small patches used in our stimulus is highly sensitive to the initial fMRI defined source placement. We attribute the need for the constrained search as being due to slight inaccuracies in the fMRI localization plus our representing each patch by a single dipole rather than by the integral of the dipoles within a patch. In Fig. 7 the responses after completing the search are plotted. The time function consistency we see across hemispheres lends confidence that the true temporal activations are being extracted. Since our method has redundancy across hemispheres and to some extent across rings (i.e. the time functions for adjacent rings should be very similar) we can compare these responses in order to validate our solutions. Most source localization methods do not provide a way to check the solution validity. When inconsistencies appear as in the foveal inner ring data of both subjects we know an error has occurred, maybe in either the fMRI mapping or forward modeling procedures. It is expected that accurate foveal responses will be difficult to extract since the foveal confluence has been a difficult area to extract accurate retinotopic mappings using standard fMRI stimuli. Without accurate mapping, the sources will be constrained to the wrong surface location resulting in inappropriate temporal functions.

This new method rests on the assumption that to disambiguate the response from V1 and V2 it is necessary to have an accurate retinotopic map of the visual cortex. To further test the importance of using fMRI data we tested the sensitivity by introducing an artificial error in the retinotopic mapping. This was done by rigidly translating all the source locations by 7 mm along the fMRI flat map surface. This shift is small enough that the fMRI map still largely overlaps with the true retinotopic cortex, but since the dipoles are constrained to the orientation of the cortex it introduces a possibly large error in the source orientation. Except for the 7 mm shift of

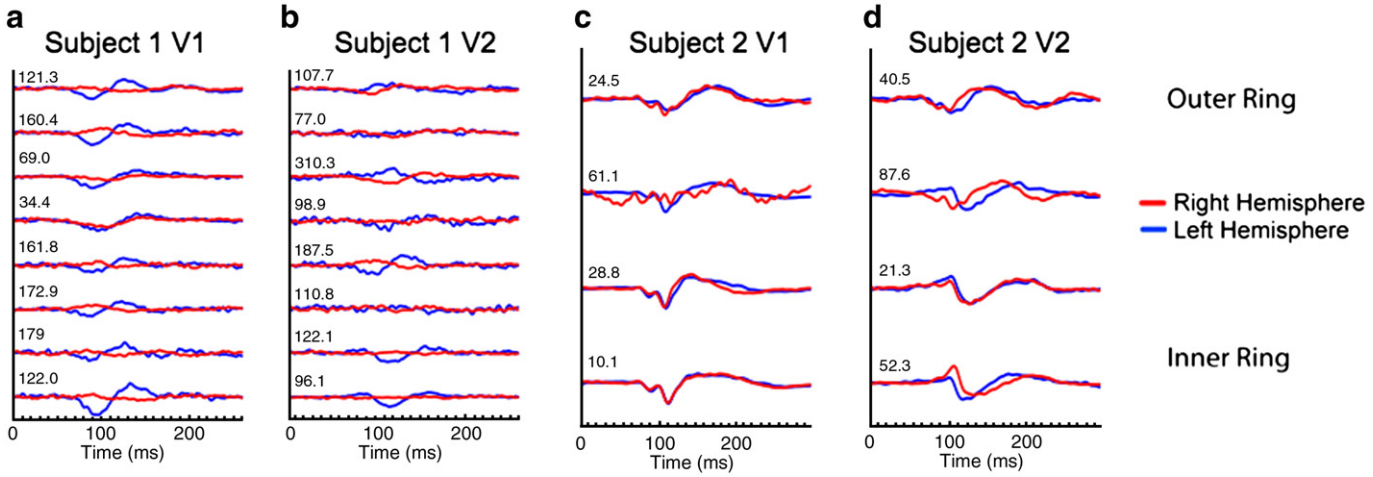

Fig. 6. Initial time function estimates. This figure shows the initial estimated time functions for V1 and V2 for each hemi-ring before the search algorithm. The red and blue indicate right and left hemisphere estimates. The number next to each waveform is the percent cross hemisphere difference. Plotted in a and b are the V1 and V2 responses for subject 1. Plotted in c and d are the responses for subject 2.

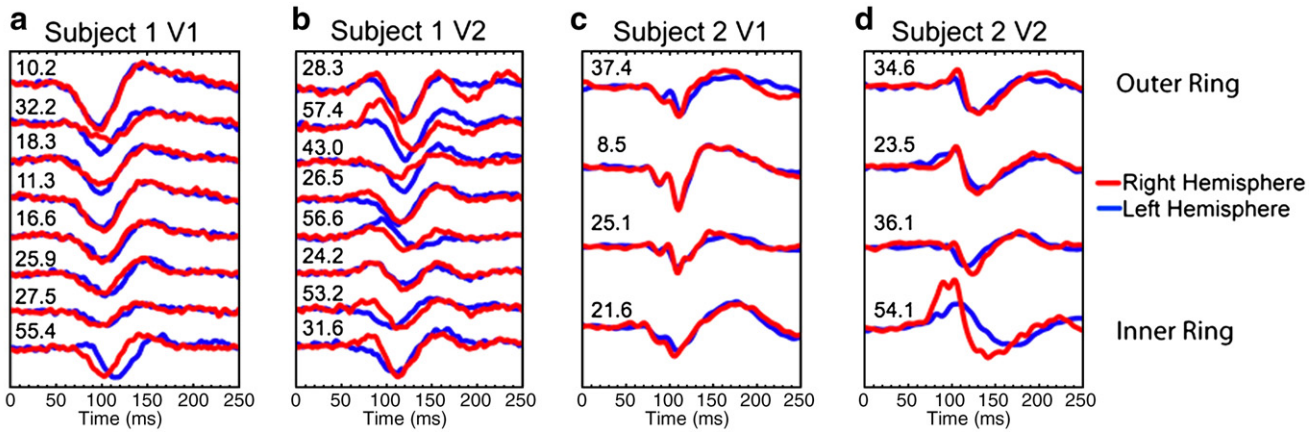

Fig. 7. V1 and V2 responses. Each panel of this figure shows the extracted waveforms from the linear regression on each hemi-ring of the stimulus with outer ring responses on the top, and the inner ring responses on the bottom. The red is the right hemisphere response and the blue is the left hemisphere response. Plotted in a and b are the V1 and V2 responses for subject 1. Plotted in c and d are the responses for subject 2. The data contributing to each hemi-ring are totally independent of each other, yet one sees consistency across hemispheres and across rings.

initial conditions for the search the method of extracting the time functions is identical to that previously described. The results of this procedure are plotted in Fig. 8. The time courses extracted are attenuated, and the consistency between hemispheres and stimulus rings disappears. For shifts less than 7 mm results were also degraded, but less so. This result shows that the fMRI data is crucial in isolating the V1 and V2 temporal responses.

As discussed, increasing the number of stimulus patches reduces the impact of noise. Accordingly, including all 192 patches in the regression will help but at the same time it could suffer from time function changes as a function of eccentricity (Baseler and Sutter, 1997). Keeping this idea in mind, Fig. 9 shows the results of assuming a common time function for the entire dataset for estimating the V1 and V2 responses (192 and 96 patches for subjects 1 and 2). Fig. 9 facilitates comparison of the V1 and V2 temporal response within and between subjects, for a given visual area both subjects have similar onset and peak latencies, providing further validation of our method.

Discussion

Previous methods of identifying multiple sources work well but only if the sources are well-separated dipoles. We have presented a method that addresses the problem of separating out responses from very close sources as in areas V1 and V2. A critical component of this method is the use of many stimulus patches. In principle, the response to a single patch would be sufficient if the following four conditions are met: (1) The VEP has a minimum of two SVD components well above the noise level (aka: a rotating dipole), (2) the fMRI is excellent so that the patch location in V1 and V2 is unambiguous, (3) the MRI is excellent so that the surface normal represents the dipole orientation and (4) the forward head model is excellent with proper conductivity estimates. However, patches often lack rotating dipoles, e.g. along the vertical meridian. Moreover, errors in estimating the cortical orientation from the fMRI/MRI are easily made in the highly convoluted occipital cortex as are errors in the forward model due to ignoring inhomogeneities in cortex and in estimating the conductivity variations of the skull. Since the four conditions are rarely satisfied the estimate of the projection of the predicted head model onto the data will be off, resulting in errors in the estimated time functions. To minimize these errors we have found that grouping 12 patches in a hemi-ring together is very helpful for averaging out the errors and finding stable time functions.

In addition to minimizing errors in the MRI/fMRI and forward model, the use of 12 patches in a hemi-ring improves the condition number of the forward model matrix $A(\mathbf{d}_{e,p}, s)$. The forward matrix has 96×12 rows corresponding to the number of electrodes times the number of patches in a hemi-ring. The number of columns is 2, corresponding to V1 and V2 dipoles. The condition number, given by

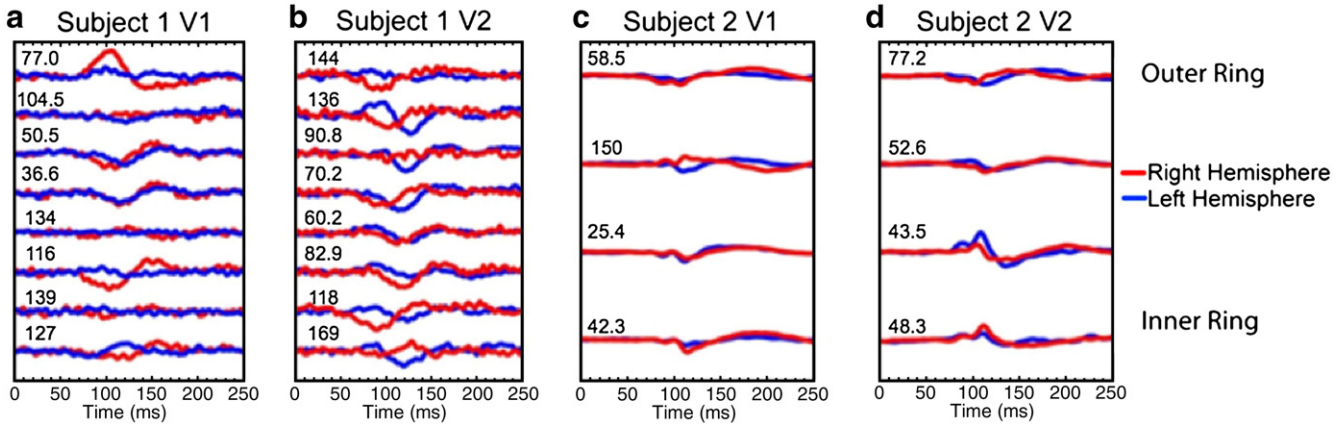

Fig. 8. Responses after shift of fMRI mapping. This figure is the same as Fig. 3 except that a mismatch between the fMRI and the EEG has been introduced by rigidly shifting the flat map correspondences by 7 mm. Compared with Fig. 7 the responses are attenuated and generally inconsistent across hemispheres.

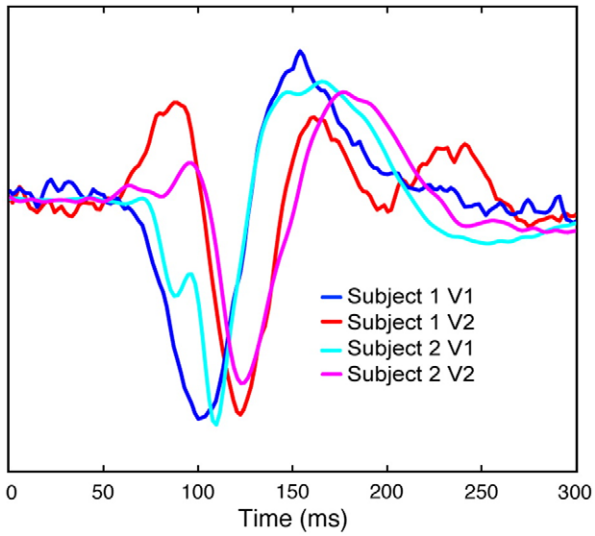

Fig. 9. Responses derived from the whole visual field. Plotted in blue and cyan are the V1 responses, with red and magenta for the V2 responses. The solid colors (blue and red) are for subject 1, with cyan and magenta for subject 2. In the legend we also included a quantification of the total percent RMS analogous to the previous plots.

the ratio of the two eigenvalues of the SVD of A, is a measure of the independence of the V1 and V2 topographies. The closer the condition number is to 1 the more trustworthy is the linear regression that is used to estimate the time functions. When 12 patches per hemi-ring are used, the poorest condition number across both subjects (16 hemi-rings for S1 and 8 for S2) was 1.5, for the closely spaced V1 and V2 dipoles. This is a good condition number. For single patches the worst condition number was >30. Condition numbers over 10 mean that 99% of the variance can be accounted for by a single dipole. These considerations provide further evidence for the need to use a large number of patches for estimating the time functions.

Because of this inherent ambiguity of these localized sources various methods have been suggested for ascertaining the identity of the dipoles. One method used by several investigators (Clark et al., 1995; Vanni et al., 2004; Zhang and Hood, 2004) is to use multiple stimulus locations and try to identify a source component that has opposite topographic polarities for stimuli in the upper versus lower hemifields. Anatomically V1 is identified by the calcarine sulcus, with a retinotopy that predicts a flip in the orientation of a dipolar source as it moves around the sulcus. This gives a good prior on how a V1 source should behave, however it is not diagnostic of a pure V1 source, since as long as the response contains more than 50% V1 there will be a flip in its orientation. As a result this heuristic is not adequate for isolating the V1 component of the waveform.

Our method uses not just a general cruciform model for the shape of the calcarine sulcus, but rather each individual subject's unique folding fingerprint to identify the locus of the VEP. Another recent paper (Hagler et al, 2008) also uses an individual subject's retinotopic organization, plus the Slotnick et al. (1999) common time function as constraints on source locations. The common time function assumption is crucial for obtaining separation of closely spaced sources. Since different patches have different mixtures of sources the benefit of using multiple stimulus locations is more than simple averaging of statistical errors, in that multiple patches make the condition number of $A(\mathbf{d}_{e,p}, s)$ approach 1. However, if the response varies as a function of stimulus location a common time function constraint will force a single time course to fit the underlying heterogeneous responses. Unlike Hagler et al. (2008) our algorithm loosened the strict retinotopic constraint by allowing the dipoles to move slightly from their initial fMRI determined location. In addition, our stimulus is much denser (192 or 96 vs. 16 stimulus patches) than that of Hagler, and allows us to compare across hemispheres and across eccentricities to verify the extracted time courses. Without that validation step it is difficult to assess the robustness of the results. Given the differences in the stimuli, it is gratifying to see similarities between our estimates of the V1 and V2 time functions and those of Hagler et al.

We can use these estimated time courses to address the controversy over which visual areas contribute to the early C1 component of the VEP, with various authors claiming either V1 or V2 is dominant (Di Russo et al., 2002). The reason for this controversy is that disambiguating the sources of activity in early visual cortex is a very difficult because of the above mentioned rotation problem. One of the very best demonstrations of the difficulty of isolating the components is provided in Fig. 6A of Hagler et al. (2008). They do cortically constrained V1/V2/V3 dipole fitting to each of their 16 stimulus patches. The 16 time functions seem to be random combinations multiple waveforms. Their Fig. 6B is much more impressive looking since the 16 waveforms (from one iso-eccentric ring) look similar to each other. However, that similarity is a tautology of enforcing a smoothness constraint, so that the result could not have been different from what is shown. We argue in order to demonstrate reliable estimate of a V1 (or V2) time function, totally independent estimates of that function are required, such as what we did in our Fig. 7 with 16 separate estimates (8 rings, right and left hemispheres) for Subject 1 and 8 separate estimates (4 rings, right and left hemispheres) for the V1 and V2 sources.

In Fig. 9 are V1 and V2 responses derived from applying the linear regression in Eq. (3) to the whole field, rather than hemirings. The initial V1 and V2 responses have similar latencies, but opposite polarities. The recorded signal at each electrode is some linear mixture of these sources, which will still exhibit a large initial negative peak that still obeys the general rules as to the assumed shape of the calcarine fissure. However based on our results we argue that this peak, while partially reflecting the V1 signal, will be contaminated with different amounts of other sources depending on stimulus configuration and a subject's individual folding pattern. This is why it is important to have a method with an internal consistency check to verify the purity of source reconstruction. In view of the hierarchy of visual areas it is often assumed that V1 responds earlier than V2, and the fact that V1 and V2 show similar initial latencies in our reconstructions might seem strange. However, depth electrodes in macaque V1 and V2 show a similar VEP profile to the responses in Fig. 6, with V1 and V2 waveforms having opposite polarities and similar onset timings (Mehta et al., 2000). While single cell recordings may reveal different V1 and V2 latencies for the quickest initially arriving spikes (Schmolesky et al., 1998), they also find that the distribution of responses across all cells in each area has a large overlap of timings. We contend that the EEG signal, which is a mass response from many cells, indicates nearly identical response latency in the two areas. Using methods similar to ours, another group has recently found V1 and V2 time functions that closely match those reported here (Goh XL, Vanni L, Henriksson L, James AC, Annual Meeting of the Organization for Human Brain Mapping 2009) providing further validation for this general approach to source identification. Our results (Fig. 9) on two subjects are also in good agreement with Hagler et al.'s (2008) Fig. 7 on two subjects. All four V1 waveforms are similar. Our V2 waveforms with a small initial positive deflection followed by a deep negative deflection are similar to the summation of Hagler et al.'s V2 plus V3. It is indeed possible that since we didn't include V3 in our analysis, its contribution could have leaked into the V2 response.

A conclusion that can be taken from our study is that there are good reasons to believe that the approach of using fMRI/MRI constrained dipole orientations together with a common time

function for multiple patches at a given eccentricity is on the path to giving trustworthy estimates of the responses in tightly packed visual areas with high temporal resolution. Possible future improvements to this method include extending the mapping to other retinotopic areas beyond V1and V2. This disambiguation procedure should also be extendable to arbitrary stimuli placed in known retinotopic locations. It is our hope that these methods can be used to address how stimulus selectivity arises in time across multiple visual areas. Distinguishing between feedforward and feedback processes is very difficult without high resolution in both space and time. Knowing where and when stimulus selectivity arises provides a useful tool for analysis of neural information processing.

Appendix A. Supplementary data

Supplementary data associated with this article can be found, in the online version, at doi:10.1016/j.neuroimage.2009.09.022.

References

Baillet, S., Riera, J.J., Marin, G., Mangin, J.F., Aubert, J., Garnero, L., 2001. Evaluation of inverse methods and head models for EEG source localization using a human skull phantom. Phys. Med. Biol. 46 (1), 77–96.

Baker, S., Baseler, H., Klein, S., Carney, T., 2006. Localizing sites of activation in primary visual cortex using visual-evoked potentials and functional magnetic resonance imaging. J. Clin. Neurophysiol. 23, 404–415.

Baseler, H.A., Sutter, E.E., 1997. M and p components of the vep and their visual field distribution. Vision Res. 37 (6), 675–690.

Baseler, H.A., Morland, A.B., Wandell, B.A., 1999. Topographic organization of human visual areas in the absence of input from primary cortex. J. Neurosci. 19 (7), 2619–2627.

Carney, T., Ales, J. and Klein, S.A., 2006. Advances in multifocal methods for imaging human brain activity. Proceedings of SPIE “Human Vision and Electronic Imaging X1” 6057, pp. 16-1 16-12.

Clark, V., Fan, S., Hillyard, S., 1995. Identification of early visual evoked potential generators by retinotopic and topographic analyses. Hum. Brain Mapp. 2 (3), 170–187.

Dale, A.M., Fischl, B., Sereno, M.I., 1999. Cortical surface-based analysis. I. segmentation and surface reconstruction. Neuroimage 9 (2), 179–194.

Dale, A.M., Liu, A.K., Fischl, B.R., Buckner, R.L., Belliveau, J.W., Lewine, J.D., et al., 2000. Dynamic statistical parametric mapping: combining fMRI and meg for high-resolution imaging of cortical activity. Neuron 26 (1), 55–67.

Dandekar, S., Ales, J., Carney, T., Klein, S.A., 2007. Methods for quantifying intra-and inter-subject variability of evoked potential data applied to the multifocal visual evoked potential. J. Neurosci. Methods 165, 270–286.

DeYoe, E.A., Bandettini, P., Neitz, J., Miller, D., Winans, P., 1994. Functional magnetic resonance imaging (fMRI) of the human brain. J. Neurosci. Methods 54 (2), 171–187.

Di Russo, F., Martínez, A., Sereno, M.I., Pitzalis, S., Hillyard, S.A., 2002. Cortical sources of the early components of the visual evoked potential. Hum. Brain Mapp. 15 (2), 95–111.

Dougherty, R.F., Koch, V.M., Brewer, A.A., Fischer, B., Modersitzki, J., Wandell, B.A., 2003. Visual field representations and locations of visual areas v1/2/3 in human visual cortex. J. Vis. 3 (10), 586–598.

Engel, S.A., Glover, G.H., Wandell, B.A., 1997. Retinotopic organization in human visual cortex and the spatial precision of functional MRI. Cereb. Cortex 7 (2), 181–192.

Ferree, T.C., Clay, M.T., Tucker, D.M., 2001. The spatial resolution of scalp EEG. Neurocomputing 38 (40), 1209–1216.

Fischl, B., Sereno, M.I., Tootell, R.B., Dale, A.M., 1999. High-resolution intersubject averaging and a coordinate system for the cortical surface. Hum. Brain Mapp. 8 (4), 272–284.

Goncalves, S.I., de Munck, J.C., Verbunt, J.P.A., Bijma, F., Heethaar, R.M., Lopes da Silva, F., 2003. *In vivo* measurement of the brain and skull resistivities using an EIT-based method and realistic models for the head. Biomedical. Engineering, IEEE Transactions on 50 (6), 754–767.

Horton, J.C., Hoyt, W.F., 1991. The representation of the visual field in human striate cortex. a revision of the classic Holmes map. Arch. Ophthalmol. 109 (6), 816–824.

Hagler, D.J., Halgren, E., Martinez, A., Huang, M., Hillyard, S.A., Dale, A.M., 2008. Source estimates for MEG/EEG visual evoked responses constrained by multiple, retinotopically-mapped stimulus locations. Hum. Brain Mapp. 2008 20 Jun.

Hämäläinen, M.S., Ilmoniemi, R.J., 1994. Interpreting magnetic fields of the brain: minimum norm estimates. Med. Biol. Eng. Comput. 32 (1), 35–42.

Klein, S.A., Carney, T., 1995. The usefulness of the laplacian in principal component analysis and dipole source localization. Brain Topogr. 8 (2), 91–108.

Lütkenhöner, B., 1998. Dipole separability in a neuromagnetic source analysis. IEEE Trans. Biomed. Eng. 45 (5), 572–581.

Mehta, A.D., Ulbert, I., Schroeder, C.E., 2000. Intermodal selective attention in monkeys. I: distribution and timing of effects across visual areas. Cereb. Cortex 10 (4), 343–358.

Mosher, J.C., Leahy, R.M., Lewis, P.S., 1999. Eeg and meg: forward solutions for inverse methods. IEEE Trans. Biomed. Eng. 46 (3), 245–259.

Mosher, J.C., Spencer, M.E., Leahy, R.M., Lewis, P.S., 1993. Error bounds for eeg and meg dipole source localization. Electroencephalogr. Clin. Neurophysiol. 86 (5), 303–321.

Nunez, P.L., Srinivasan, R., 2006. Electric fields of the brain: the neurophysics of eeg. Oxford University Press, New York.

Phillips, C., Rugg, M.D., Friston, K.J., 2002. Anatomically informed basis functions for eeg source localization: combining functional and anatomical constraints. Neuroimage 16 (3 Pt. 1), 678–695.

Scherg, M., 1992. Functional imaging and localization of electromagnetic brain activity. Brain Topogr. 5 (2), 103–111.

Schira, M.M., Wade, A.R., Tyler, C.W., 2007. Two-dimensional mapping of the central and parafoveal visual field to human visual cortex. J. Neurophysiol. 97 (6), 4284–4295.

Schmolesky, M.T., Wang, Y., Hanes, D.P., Thompson, K.G., Leutgeb, S., Schall, J.D., et al., 1998. Signal timing across the macaque visual system. J. Neurophysiol. 79 (6), 3272–3278.

Sharon, D., Hamalainen, M.S., Tootell, R.B., Halgren, E., Belliveau, J.W., 2007. The advantage of combining MEG and EEG: comparison to fMRI in focally stimulated visual cortex. Neuroimage 36, 1225–1235.

Slotnick, S.D., Klein, S.A., Carney, T., Sutter, E., Dastmalchi, S., 1999. Using multi-stimulus vep source localization to obtain a retinotopic map of human primary visual cortex. Clin. Neurophysiol. 110 (10), 1793–1800.

Sutter, E.E., 1991. The fast m-transform: a fast computation of cross-correlations with binary m-sequences. SIAM J. Comput. 20 (4), 686–694.

Sutter, E.E., 2001. Imaging visual function with the multifocal m-sequence technique. Vision Res. 41 (10-11), 1241–1255.

Teo, P.C., Sapiro, G., Wandell, B.A., 1997. Creating connected representations of cortical gray matter for functional MRI visualization. IEEE Trans. Med. Imaging 16 (6), 852–863.

Vanni, S., Warnking, J., Dojat, M., Delon-Martin, C., Bullier, J., Segebarth, C., 2004. Sequence of pattern onset responses in the human visual areas: an fMRI constrained VEP source analysis. Neuroimage 21 (3), 801–817.

Zhang, Z., 1995. A fast method to compute surface potentials generated by dipoles within multilayer anisotropic spheres. Physics in medicine and biology 40 (3), 335–349.

Zhang, X., Hood, D.C., 2004. A principal component analysis of multifocal pattern reversal vep. J. Vis. 4 (1), 32–43.

Zhang, Z., Jewett, D.L., Goodwill, G., 1994. Insidious errors in dipole parameters due to shell model misspecification using multiple time-points. Brain Topogr. 6 (4), 283–298.